

# Using Voronoi Tessellations to Assess Nanoparticle–Nanoparticle Interactions and Ordering in Monolayer Films Formed through Electrophoretic Deposition

Alex J. Krejci,<sup>†,‡</sup> Colin G. W. Thomas,<sup>†,‡</sup> Jyotirmoy Mandal,<sup>†,‡</sup> Isabel Gonzalo-Juan,<sup>†,‡</sup> Weidong He,<sup>‡,§</sup> Ryan L. Stillwell,<sup>||</sup> Ju-Hyun Park,<sup>||</sup> Dhiraj Prasai,<sup>‡,§</sup> Vyacheslav Volkov,<sup>⊥</sup> Kirill I. Bolotin,<sup>†,‡</sup> and James H. Dickerson<sup>\*,†,‡,○</sup>

<sup>†</sup>Department of Physics and Astronomy, Vanderbilt University, Nashville, Tennessee 37235, United States

<sup>‡</sup>Vanderbilt Institute for Nanoscale Science and Engineering, Vanderbilt University, Nashville, Tennessee 37235, United States

<sup>§</sup>Interdisciplinary Graduate Program in Materials Science, Vanderbilt University, Nashville, Tennessee 37235, United States

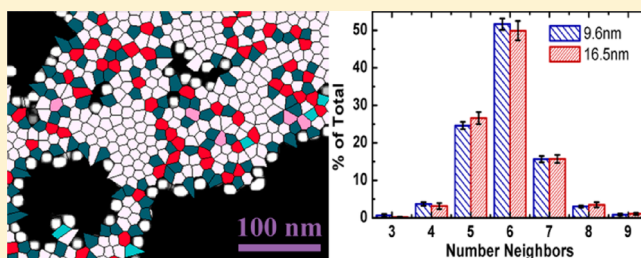
<sup>||</sup>National High Magnetic Field Laboratory, Florida State University, Tallahassee, Florida 32310, United States

<sup>⊥</sup>Condensed Matter Physics and Material Science Department, Brookhaven National Laboratory, Upton, New York 11973, United States

<sup>○</sup>Department of Chemistry, Vanderbilt University, Nashville, Tennessee 37235, United States

## **S** Supporting Information

**ABSTRACT:** Monolayers of iron oxide nanoparticles of two different sizes, 9.6 nm and 16.5 nm, were fabricated through electrophoretic deposition. The arrangements of nanoparticles within the films were analyzed using the technique of Voronoi tessellations. These analyses indicated that the films possessed equivalent degrees of ordering, and that the films were uniform over centimeter length scales. Precise measurements of the interparticle spacing were obtained, and the magnitudes of magnetic dipole interactions were calculated. The dipole–dipole interaction among the larger nanoparticles was 14 times larger than that of the smaller nanoparticles, indicating that magnetic coupling interactions could not have been the lone source of ordering in the system.



## **I** INTRODUCTION

Controlling the nanostructure of monolayer films of nanoparticles (NPs) is critical for the application of these films to technologies such as magnetic storage media and photovoltaics.<sup>1</sup> In addition to interest in these technological applications, new physical phenomena may emerge from NP monolayer formation when individual nanoparticles assemble into films and coatings at mesoscopic and macroscopic scales.<sup>2–5</sup> Control over the nanostructure demands an understanding of the particle–particle interactions within the film. These particle–particle interactions play an important role in administering the nanoscale ordering among the NPs in the film.<sup>6</sup> To help elucidate the significance of both the particle–particle interactions and the ordering within NP films, we can analyze these structures, using Voronoi tessellations. Voronoi tessellations (or Voronoi diagrams) have a long history of use in a variety of fields, including anthropology, astronomy, biology, chemistry, computational geometry, physics, and statistics.<sup>7–9</sup> A Voronoi tessellation, as defined by Okabe, is an association, “...given a set of two or more but a finite number of distinct points in the Euclidean plane, ...” of “...all locations in that space with the closest member(s) of the point set with

respect to the Euclidean distance”.<sup>7</sup> On the basis of this definition, all closed, associated regions within the Voronoi tessellation in two dimensions will consist solely of  $n$ -sided polygons. The number of sides of the polygon ( $n$ ) represents the number of nearest neighbors each corresponding NP has, thus indicating the type and the extent of ordering of nanoparticles within the film.

In this article, we introduce the use of the Voronoi tessellation as a means of studying monolayer films of nanoparticles, fabricated by electrophoretic deposition (EPD). Because of the clear visual assessment that can be made about the degree of ordering within an ensemble from examining Voronoi diagrams and because of the numerical metrics that can be calculated from said diagrams, the Voronoi tessellations will facilitate qualitative and quantitative analyses of nanoparticle monolayers, which provide insight into the basic

**Special Issue:** Electrophoretic Deposition

**Received:** June 17, 2012

**Revised:** August 16, 2012

processes occurring during monolayer formation.<sup>10</sup> Qualitatively, the diagram allows for easy visualization of the nature of NPs. Given that two of the most common ordered arrangements of spherical nanoparticles in two dimensions are cubic packing and hexagonal packing, the Voronoi tessellation would indicate these types of packing by the presence of polygons with four or six sides, respectively. The image of the Voronoi tessellation, then, would show readily where within a film such types of NP packing occur. Quantitatively, the number of sides and the locations of Voronoi vertices would play a critical role in measuring both the degree of ordering in the film and the center-to-center spacing (CtC) between NPs. Both of these quantities must be ascertained to govern ordering within a monolayer film or a multilayer film of nanoparticles.

## EXPERIMENTAL SECTION

Two diameters of nanoparticles were synthesized for this study using a previously published procedure.<sup>11,12</sup> Suspensions of the iron oxide nanoparticles, used for EPD, were prepared by dispersing the NPs in hexane with a resulting concentration of 1 mg/mL. The NPs were characterized using a variety of techniques to determine their chemical, structural, and magnetic properties. High-resolution transmission electron microscopy (TEM) was conducted on a JEOL JEM2100F microscope and on a Philips CM200 microscope, both operating at 200 kV. TEM samples for the Philips CM200 were prepared on a copper grid with ultrathin carbon type-A film (Ted Pella, Inc.); samples for the JEOL JEM2100F were prepared using a gold grid with a single sheet of graphene, fabricated entirely in house. X-ray diffraction (XRD) measurements on powders of NPs, cast onto a zero-background Si(511) substrate, were obtained using a Scintag X<sub>1</sub> Powder X-ray Diffractometer under irradiation from a Cu K $\alpha$  source ( $\lambda = 1.5406 \text{ \AA}$ ). Absorption spectroscopy was conducted on a Varian Cary 5000 UV–vis/NIR spectrophotometer. Magnetic characterization measurements were obtained using vibrating sample magnetometry (VSM) on a Quantum Design PPMS system. A Malvern Zetasizer Nano ZS was used to measure the electrophoretic mobility and hydrodynamic diameter of our nanoparticle suspensions by means of laser Doppler velocimetry and dynamic light scattering (DLS).

NP films were deposited using electrophoretic deposition (EPD). Two epi-ready, phosphorus-doped, silicon wafers (n-type, MEMC Electronic Materials SDN) with extant native oxide surface layers of dimensions  $\sim 5.0 \text{ cm} \times 0.5 \text{ cm}$  were used as electrodes. These wafers were positioned in a parallel plate capacitor configuration with a 5 mm wide gap between them. A 500 V potential was applied across the electrodes using a Keithley 2410 electrometer, after which the electrodes were inserted into the NP and hexane suspension. After the desired deposition time, the electrodes were extracted. The 500 V potential remained for approximately 1 min after said extraction. Films were characterized using scanning electron microscope (SEM) images, acquired on a Raith e-Line electron-beam lithography instrument, operating in SEM mode at 10 kV. All Voronoi tessellation analyses were conducted on at least five SEM micrographs, each of which surveyed over  $700\,000 \text{ nm}^2$ , selected from random locations across the films.

## DISCUSSION AND RESULTS

Two sizes of nanoparticles,  $9.6 \pm 0.9$  and  $16.5 \pm 1.2 \text{ nm}$  as measured from TEM images, were separately studied. The

XRD data, shown in Figure 1a, indicated the presence of FeO (wüstite JCPDF #46-1312) and either  $\gamma\text{-Fe}_2\text{O}_3$  (maghemite

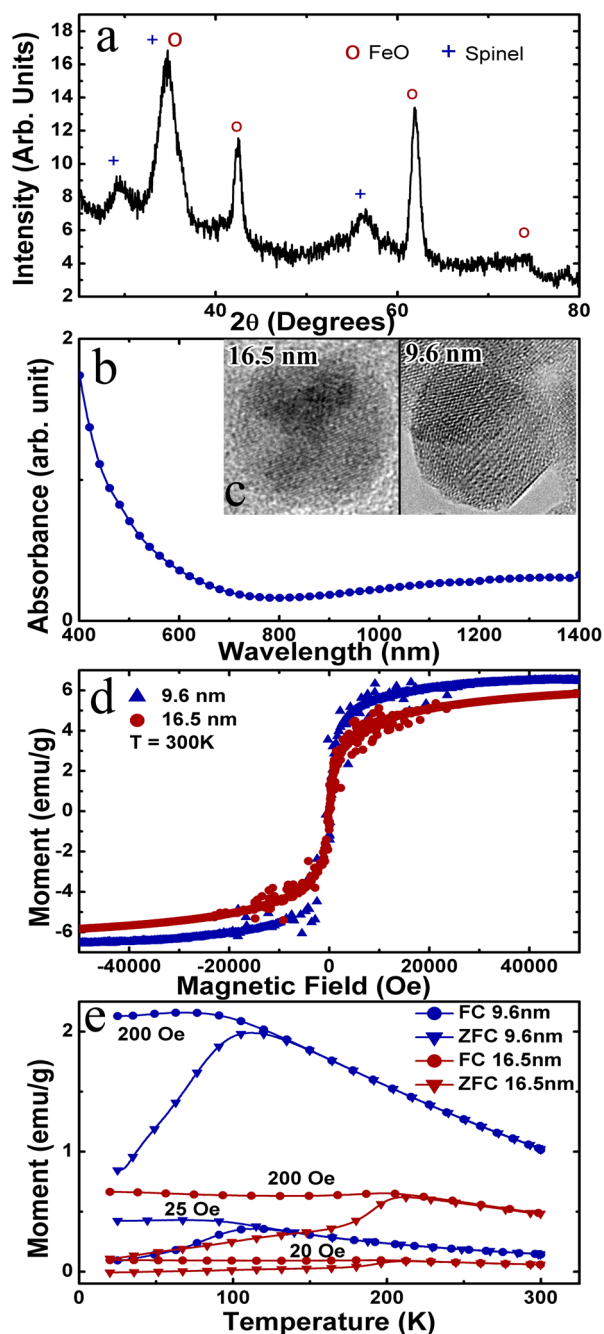


**Figure 1.** (a) Representative XRD data indicating the presence of the FeO phase and either the  $\text{Fe}_3\text{O}_4$  phase or the  $\gamma\text{-Fe}_2\text{O}_3$  phase of iron oxide in the NPs. (b) Complementary absorption spectroscopy data distinguished the existence of  $\text{Fe}_3\text{O}_4$  in the NPs. (c) TEM micrographs of the two NPs. (d) Magnetization hysteresis curves confirmed the superparamagnetic nature of both NPs. (e) FC and ZFC data provided additional evidence of the superparamagnetic behavior of NPs.

JCPDF #39-1346) or  $\text{Fe}_3\text{O}_4$  (magnetite JCPDF #19-0629) in the NPs. Absorption spectroscopy provided complementary information that differentiated maghemite and magnetite; Figure 1b confirmed the presence of  $\text{Fe}_3\text{O}_4$  in the NPs.<sup>13</sup> TEM micrographs show the single crystal nature of both diameters of NPs (Figure 1c).

Magnetic hysteresis curves (Figure 1d) in combination with FC/ZFC data (Figure 1e) of NPs of both sizes confirmed the superparamagnetic nature of the NPs. The magnetic moment of a single NP was calculated per force to understand the strength of the magnetic interaction between two NPs. To calculate the respective moments, the masses were first computed ( $\sim 2.5 \times 10^{-18}$  g/particle for 9.6 nm particles and  $\sim 1.3 \times 10^{-17}$  g/particle for 16.5 nm particles) using the average density of wüstite and magnetite multiplied by the volume of a sphere, incorporating the radius measured from TEM images.<sup>14</sup> Then, from the saturation magnetization and the total sample mass, the moments for the NPs were determined to be  $1800 \pm 100 \mu_B$  for the 9.6 nm NPs and  $8600 \pm 100 \mu_B$  for the 16.5 nm particles, where  $\mu_B$  is the Bohr magneton.

One main objective of using Voronoi analysis to study the monolayer films was to assess particle–particle interactions by way of quantifying the ordering of the film. However, ordering in NP monolayers occurs not only through particle–particle interactions but also through constraint forces dictated by boundary conditions on the NPs in three dimensions, capillary forces during the evaporation of the solvent used in the EPD suspension, and particle–substrate interactions, among other forces.<sup>4,5,15</sup> All of the cited forces that facilitate ordering are central to the successful production of ordered NP arrays, using evaporative self-assembly, ligand-mediated assembly, and Langmuir–Blodgett techniques, three alternative techniques used to form NP monolayer films.<sup>16–20</sup> In EPD, nanoparticles can move freely in the plane perpendicular to the electric field; therefore, constraint forces dictated by boundary conditions cannot alone instigate ordering. Also, NPs deposit well before the EPD solvent evaporates, which eliminates capillary forces as a predominant faction that causes ordering. Thus, the remaining proposed ordering mechanisms, particle–particle and particle–substrate interactions, administrate NP ordering in films fabricated using EPD.<sup>21</sup> The silicon substrates used in these experiments possess surface topology, which is negligible compared to the diameter of each NP, including the steady state length of the ligands that coat the NPs. Therefore, we assert that all particle–substrate interactions must be isotropic in the plane parallel to the substrate. From the isotropic nature of the substrate, we infer that, while particle–substrate interactions may influence ordering within the film, particle–substrate interactions alone cannot bring about ordering. Thus, the existence of ordering is primarily due to particle–particle interactions. The presence and absence of ordering in NP monolayers formed by EPD has been observed previously.<sup>12,22,23</sup> In each of these instances, for which order was observed, the existence of a dominant particle–particle interaction (van der Waals, dipolar interactions, Coulomb interactions, etc.) was conjectured to be the root cause of the phenomenon. In our study, we believe that van der Waals (vdW) interactions and magnetic dipolar interactions are the predominant forces that govern the observed ordering within our iron oxide NP monolayer films.

Figure 2a shows the electrophoretic mobility measurements of our hexane-based suspensions. The as-synthesized NPs suspended in hexane tended to have very low absolute electrophoretic mobility. Therefore, to enhance the electrophoretic mobility of the NPs, we employed a processing step that removed a portion of the surfactant molecules from the nanocrystals. The procedure of removing surfactant molecules from the nanocrystals yielded charges on their surface, as they were suspended in nonpolar solvents.<sup>18,24</sup> The process involved

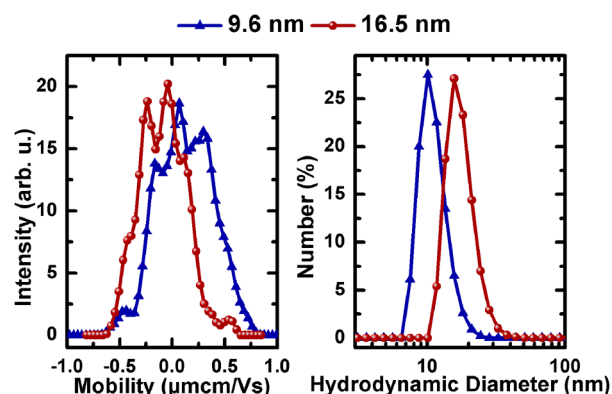


**Figure 2.** (a) Electrophoretic mobility measurements revealed the presence of a distribution of positively and negatively charged nanoparticles within the EPD suspensions. (b) Dynamic light scattering data, taken from the EPD suspensions, indicated the nanoparticles were singly suspended in hexane, since the measured diameters for both NPs were similar, within the measured uncertainty, to the diameters measured from the TEM micrographs.

liquid–liquid extraction with the mixture ethanol:hexane (9:1) to remove the residues of the synthesis. Thereafter, the NPs were isolated, resuspended in hexane, and centrifuged. After this procedure, the mobility of the NPs increased notably to the values displayed in Figure 2a. Such distributions of both negatively and positively charged NPs are characteristic of NP suspensions in nonpolar solvents.<sup>14,18,22,25,26</sup> The suspended objects were ostensibly NP monomers, as evidenced by DLS data that indicated the presence of objects with an average hydrodynamic diameter approximately equivalent to the diameter of the NPs measured using TEM images (Figure 2b).

To calculate the strength of the magnetic dipole and vdW interactions between NPs, the center-to-center spacing between the NPs must be ascertained. CtC can be determined from SEM images by identifying the locations of all particles within the image (Figure S1, Supporting Information). The set of all NP locations also allows for the Voronoi tessellation analyses of the films that, in turn, will be used to assess the ordering of the film (Figure 3, Figure S2, Supporting Information). Two methods were used to measure the CtC between particles. The first method utilized the radial distribution function (RDF), a function that described how the density of particles varied as a function of distance from a reference particle (Figure 4a).<sup>27–31</sup> In a system of hexagonally packed particles, the first five maxima in the RDF occur at factors of  $1\times$ ,  $\sqrt{3}\times$ ,  $2\times$ ,  $\sqrt{7}\times$ , and  $3\times$  the average CtC between two nearest-neighboring particles.<sup>30</sup> The RDF was determined by first counting the number of particles that resided within concentric rings of increasing radii, centered at the middle of a given particle; the result of this tally was a data set of intensity (number of particles) as a function of radius. The step size of the increasing radii corresponded to  $1/2$  pixel of the SEM, analyzed in the Voronoi tessellation. Subsequently, data sets of intensity as a function of radius were obtained for each particle that was identified within a fixed maximum ring diameter (140 pixels) within the image. At each value of the radius, the average intensity of all data sets was calculated. To average the intensities over multiple images, the expressions for the intensities as functions of the radii for each image were normalized. Numerically integrating the averaged intensities from each image over the entire range of radii and, then,



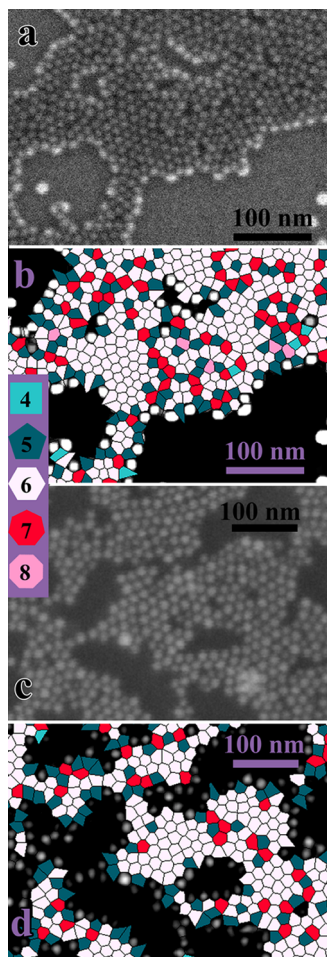


**Figure 3.** (a) SEM micrograph of a film comprised of 9.6 nm NPs. (b) Voronoi tessellation of the NP film seen in part a. (c) SEM micrograph of a film comprised of 16.5 nm NPs. (d) Voronoi tessellation of the NP film seen in part c.

dividing those same intensities by the resulting integrals normalized the functions. Before averaging the normalized data over each image, the intensities were converted to densities by dividing the normalized intensities by the area encompassed by the radial ring that defined said area. Finally, the normalized densities were averaged over each image, and the error bars were determined using the standard deviation of the normalized densities from each image. The final result was a normalized RDF averaged over multiple images. The first maximum in the RDF was fit to a Gaussian distribution function, and the mean value of the fit was used as the average CtC between nearest neighboring nanoparticles. From these assessments, the nearest neighbor CtC of  $13.4 \pm 1.5$  nm and  $16.7 \pm 1.4$  nm were determined for the 9.6 and 16.5 nm nanoparticles, respectively.

The second approach for finding the CtC between nearest neighbor NPs utilized the Voronoi tessellation. Since our interests focused exclusively on NPs that were tightly packed within the monolayer film, our Voronoi tessellation analyses considered only NPs that appeared in hexagonal arrangements. This required us to concentrate only on NPs that were represented by six-sided Voronoi cells. We further restricted the subsequent subset of NPs to include those whose Voronoi cell edge lengths were within 50% of the median edge length of the cell, as selected from the set of all observed NPs. These criteria

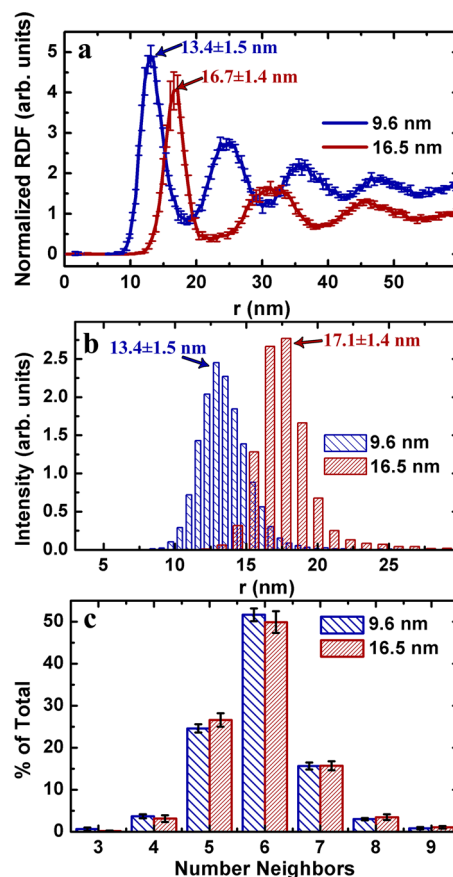


**Figure 4.** (a) Normalized, radial distribution function measured using SEM micrographs. (b) Particle spacing histogram, determined from a subset of the Voronoi tessellations. (c) Percentage of particles within the analyzed films that corresponded to a Voronoi polygon with  $n$  sides. The comparable percentages for each of the  $n$ -sided polygons suggested the presence of equivalent ordering within the 9.6 nm and 16.5 nm nanoparticle films.

limited the subset of NPs to those represented by cells that approximate an equilateral hexagon. From this refined subset of NPs, the Euclidean distance to all six neighbors of each NP in the subset was calculated using the location of the representative cell's Voronoi vertices. A histogram of all the distances is shown in Figure 4b; the mean value of this histogram was designated the CtC. From this method, CtC values of  $13.4 \pm 1.5$  nm and  $17.1 \pm 1.4$  nm were determined for the nearest-neighbor CtC of the small and large particles, respectively. Because these CtC values represent distances to nearest neighbor particles only for particles that are tightly packed, they will be used in the calculation of vdW and magnetic dipole particle–particle interaction energies.

Given the measured CtC and the magnetic moment of the particles, the magnetic dipole–dipole interaction energy was calculated using

$$E_{\text{dipole}} = \mu_0 \frac{(\vec{m}_1 \cdot \vec{m}_2 - 3(\vec{m}_1 \cdot \hat{n})(\vec{m}_2 \cdot \hat{n}))}{4\pi |x_1 - x_2|^3} \quad (1)$$

where  $\mu_0$  is the magnetic permeability of free space,  $\vec{m}_{1,2}$  are the magnetic moments of the nanoparticles,  $x_{1,2}$  are the locations of the nanoparticles, and  $\hat{n}$  is a unit vector pointing along the vector separating the two particles.<sup>32</sup> Interaction energies were calculated for two particles with dipoles oriented head to tail, the maximum attractive configuration (Table 1).

**Table 1. Particle–Particle Interaction Energies<sup>a</sup>**

	$\frac{E_{\text{dipole}}}{k_{\text{B}}T}$	$\frac{E_{\text{vdW}}}{k_{\text{B}}T}$	$\frac{E_{\text{vdW}}}{E_{\text{dipole}}}$
$d_{\text{S}} = 9.6 \text{ nm}$	−0.005	−0.06	12
$d_{\text{I}} = 16.5 \text{ nm}$	−0.06	−4.0	67
$d_{\text{I}}/d_{\text{S}}$	12	67	5.6

<sup>a</sup> $k_{\text{B}}T$  is calculated at 300 K.

The vdW interaction energy between two nanoparticles was calculated using

$$E_{\text{vdW}} = -\frac{A_{\text{pop}}}{12} \left\{ \frac{d^2}{r^2} + \frac{d^2}{r^2 - d^2} + 2 \ln \left( \frac{r^2 - d^2}{r^2} \right) \right\} \quad (2)$$

where  $A_{\text{pop}}$ ,  $d$ , and  $r$  are the Hamaker constant, particle diameter, and CtC between particles, respectively. A Hamaker constant of 137 meV, corresponding to magnetite–magnetite interactions in hexane, was used (Table 1).<sup>33</sup>

From the table, of the two sizes, the larger NPs interacted much more strongly than the smaller NPs through both vdW and magnetic dipole interactions. Also, the vdW interactions were stronger than the magnetic interactions for both nanoparticle diameters. For the larger particles, the ratio of vdW to dipolar interactions was notably larger than that of the smaller particles. This was because the NP–NP CtC was quite close to the diameter of the NP, which suggested that the vdW interaction of the larger particle was highly sensitive to small changes in CtC. Interestingly, both types of interaction energies for the smaller particles were significantly less than the associated thermal energies, although the existence of ordering remained from SEM images. This suggests that additional particle–particle interactions, such as steric interactions due to surface ligands, may have played a significant accompanying role in the formation of NP films.<sup>2</sup> Finally, the ordering of the film was assessed by measuring the percentage of all NPs that were represented by an  $n$ -sided Voronoi cell (Figure 4c). In this study,  $n$  ranged from 3 to 9. As mentioned previously,  $n = 6$  corresponded to hexagonal close packing and  $n = 4$  corresponded to cubic packing in two dimensions. The uncertainty in the histogram was calculated as the standard deviation of the percentages measured for each image of a single NP size. The small size of the error bars, ~5%, indicated that ordering within the film was consistent across size scales of up to ~1 cm<sup>2</sup>. We also calculate a measure of entropy in the system using

$$S = - \sum_{i=3}^9 p_i \ln p_i \quad (3)$$

where  $S$  is the entropy and  $p_i$  is the probability of being of a Voronoi cell having  $i$  edges.<sup>34</sup>

The histogram demonstrated that ordering within iron oxide NP films, comprised of NPs of two notably different diameters and, hence, different magnitudes of particle–particle interactions, was the same, within uncertainty. The resulting calculation yields  $1.27 \pm 0.03$  as the entropy for both particle sizes, concurring with the histogram. However, calculations of magnetic dipole and vdW interactions indicated significant differences in the magnitudes of the interactions for the two sizes. The disparity between the measure of ordering and the calculated interaction energies could be explained by the dominance of many-particle, ensemble interactions over two

particle interactions. Another possibility, to which we alluded earlier, was that steric interactions between the ligands could comprise a substantial portion of the interactions that govern ordering among the nanoparticles. These findings suggest that magnetic NPs of similar magnetic dipole moment, diameter, and steric interaction could be employed to fabricate ordered NP monolayers and multilayers at mesoscopic and macroscopic length scales. Further, Voronoi tessellation analysis is a viable technique to assess the degree of order in electrophoretically deposited films of nanoparticles.

## CONCLUSIONS

The degree of ordering and the CtC of NP monolayers, fabricated by the electrophoretic deposition of iron oxide nanoparticles of two different diameters, were determined through the Voronoi tessellation analysis of SEM micrographs. Assessment of the nanoparticles, the EPD suspension, and the resulting NP monolayers suggested that particle–particle interactions were the predominant driver of ordering in the monolayer films. Voronoi tessellation analysis allowed for the measurement of the average CtC between nearest neighbor, tightly packed NPs. Using the measured CtC in combination with magnetic data and the Hamaker constant, magnetic and vdW interactions between two neighboring particles were calculated. The resulting calculations indicated that the larger particles interact much more strongly with each other than did the smaller particles. However, the ordering in both films was measurably equivalent. Future investigations to determine the origin of ordering will incorporate nanoparticles with and without intrinsic dipole moments, which will explore the feasibility of other particle–particle interactions to govern the evolution of ordering. Nanoparticles with significantly larger dipole moments, such as ZnO doped with Co, would probe whether one dominant particle–particle force, one with a magnitude that was  $10^m \times$  larger than the other extant forces, could yield ordered NP arrangements.<sup>35</sup> Another route of investigation should consider the effect of steric interactions (due to composition, length, conformation, and other characteristics of the surface ligands) on the ordering of the NPs.

## ASSOCIATED CONTENT

### Supporting Information

Additional figures showing full SEM images after processing of 9.6 nm and 16.5 nm NPs, the same but also with Voronoi tessellation overlay, and an atomic force microscopy image of the bare, epi-ready silicon substrates used as electrodes in our experiments. This material is available free of charge via the Internet at <http://pubs.acs.org>.

## AUTHOR INFORMATION

### Corresponding Author

\*E-mail: [james.dickerson@vanderbilt.edu](mailto:james.dickerson@vanderbilt.edu).

### Author Contributions

The manuscript was written through contributions of all authors. All authors have given approval to the final version of the manuscript.

### Notes

The authors declare no competing financial interest.

## ACKNOWLEDGMENTS

This research is partially supported by the United States Office of Naval Research, Award N000140910523, the National Science Foundation (NSF) Award DMR-0757380, and Award DMR-1054161.

## REFERENCES

- (1) Talapin, D. V.; Lee, J. S.; Kovalenko, M. V.; Shevchenko, E. V. *Chem. Rev.* **2010**, *110*, 389–458.
- (2) Motte, L.; Courty, A.; Ngo, A.-T.; Lisiecki, I.; Pileni, M.-P. *Self-Organization of Inorganic Nanocrystals*; Wiley-VCH: Weinheim, Germany, 2005.
- (3) Pileni, M. P. *J. Phys. Chem. B* **2001**, *105*, 3358–3371.
- (4) *Nanocrystals Forming Mesoscopic Structures*; Pileni, M. P., Ed.; Wiley-VCH: 2005.
- (5) Pileni, M. P.; Lalatonne, Y.; Ingert, D.; Lisiecki, I.; Courty, A. *Faraday Discuss.* **2004**, *125*, 251–264.
- (6) Levesque, D.; Weis, J. J. *Phys. Rev. E* **1994**, *49*, 5131–5140.
- (7) Okabe, A.; Boots, B.; Sugihara, K.; Chiu, S. N. *Spatial Tesselations: Concepts and Applications of Voronoi Diagrams*, 2nd ed.; John Wiley & Sons Ltd: West Sussex, U.K., 2000.
- (8) Aurenhammer, F. *Computing Surveys* **1991**, *23*, 345–405.
- (9) Williams, R. E. *Science* **1968**, *161*, 276–276.
- (10) Libál, A.; Reichhardt, C.; Reichhardt, C. J. O. *Phys. Rev. E* **2007**, *75*, 011403.
- (11) Park, J.; An, K. J.; Hwang, Y. S.; Park, J. G.; Noh, H. J.; Kim, J. Y.; Park, J. H.; Hwang, N. M.; Hyeon, T. *Nat. Mater.* **2004**, *3*, 891–895.
- (12) Krejci, A. J.; Gonzalo-Juan, I.; Dickerson, J. H. *ACS Appl. Mater. Interfaces* **2011**, *3*, 3611–3615.
- (13) Kovalenko, M. V.; Bodnarchuk, M. I.; Lechner, R. T.; Hesser, G.; Schaffler, F.; Heiss, W. J. *Am. Chem. Soc.* **2007**, *129*, 6352–6353.
- (14) Kavich, D. W.; Hasan, S. A.; Mahajan, S. V.; Park, J. H.; Dickerson, J. H. *Nanoscale Res. Lett.* **2010**, *5*, 1540–1545.
- (15) Krejci, A. J.; Mandal, J.; Dickerson, J. H. *Appl. Phys. Lett.* **2012**, *101*, 043117.
- (16) Ahniyaz, A.; Sakamoto, Y.; Bergstrom, L. *Proc. Natl. Acad. Sci. U.S.A.* **2007**, *104*, 17570–17574.
- (17) Bao, Y. P.; Beerman, M.; Krishnan, K. M. *J. Magn. Magn. Mater.* **2004**, *272*, E1367–E1368.
- (18) Shevchenko, E. V.; Talapin, D. V.; Kotov, N. A.; O'Brien, S.; Murray, C. B. *Nature* **2006**, *439*, 55–59.
- (19) Lin, X. M.; Jaeger, H. M.; Sorensen, C. M.; Klabunde, K. J. *J. Phys. Chem. B* **2001**, *105*, 3353–3357.
- (20) Salzemann, C.; Richardi, J.; Lisiecki, I.; Weis, J. J.; Pileni, M. P. *Phys. Rev. Lett.* **2009**, *102*, 144502.
- (21) van der Biest, O. O.; Vandeperre, L. J. *Annu. Rev. Mater. Sci.* **1999**, *29*, 327–352.
- (22) Gonzalo-Juan, I.; Krejci, A. J.; Dickerson, J. H. *Langmuir* **2012**, *28*, 5295–5301.
- (23) Teranishi, T.; Hosoe, M.; Miyake, M. *Adv. Mater.* **1997**, *9*, 65–67.
- (24) Lee, D.; Rubner, M. F.; Cohen, R. E. *Nano Lett.* **2006**, *6*, 2305–2312.
- (25) Jia, S.; Banerjee, S.; Herman, I. P. *J. Phys. Chem. C* **2008**, *112*, 162–171.
- (26) Mahajan, S. V.; Dickerson, J. H. *Nanotechnology* **2010**, *21*, 145704.
- (27) He, D.; Ekere, N. N.; Cai, L. *Mater. Sci. Eng., A* **2001**, *298*, 209–215.
- (28) Quinn, R. A.; Cui, C.; Goree, J.; Pieper, J. B.; Thomas, H.; Morfill, G. E. *Phys. Rev. E* **1996**, *53*, R2049–R2052.
- (29) Steinhardt, P. J.; Nelson, D. R.; Ronchetti, M. *Phys. Rev. B* **1983**, *28*, 784–805.
- (30) Kaatz, F. H.; Bultheel, A.; Egami, T. *Naturwissenschaften* **2008**, *95*, 1033–1040.
- (31) Rogers, C. D. F.; Dijkstra, T. A.; Smalley, I. J. *Earth-Sci. Rev.* **1994**, *36*, 59–82.
- (32) Jackson, J. D. *Classical Electrodynamics*, 3rd ed.; John Wiley & Sons: New Delhi, India, 1999.
- (33) Faure, B.; Salazar-Alvarez, G.; Bergstrom, L. *Langmuir* **2011**, *27*, 8659–8664.
- (34) Kumar, S.; Kurtz, S. K. *Mater. Charact.* **1993**, *31*, 55–68.
- (35) Duan, L. B.; Rao, G. H.; Yu, J.; Wang, Y. C. *Solid State Commun.* **2008**, *145*, 525–528.